THE JOURNAL OF PHYSICAL CHEMISTRY C

Article

Cite This: J. Phys. Chem. C 2017, 121, 24919-24928

pubs.acs.org/JPCC

Charge-Transfer Analysis of 2p3d Resonant Inelastic X-ray Scattering of Cobalt Sulfide and Halides

Ru-Pan Wang,[†] Boyang Liu,[†] Robert J. Green,[‡] Mario Ulises Delgado-Jaime,[†] Mahnaz Ghiasi,[†] Thorsten Schmitt,[§] Matti M. van Schooneveld,*[,†] and Frank M. F. de Groot*[,†]

[†]Inorganic Chemistry & Catalysis, Debye Institute for Nanomaterials Science, Utrecht University, Universiteitsweg 99, 3584 CG Utrecht, The Netherlands

[‡]Department of Physics & Astronomy, University of British Columbia, V6T 1Z1 Vancouver, British Columbia, Canada

[§]Paul Scherrer Institut, Swiss Light Source, CH-5232 Villigen PSI, Switzerland

Supporting Information

ABSTRACT: We show that with 2p3d resonant inelastic X-ray scattering (RIXS) we can accurately determine the charge-transfer parameters of CoF_2, $CoCl_2$, $CoBr_2$, and CoS. The 160 meV resolution RIXS results are compared with charge-transfer multiplet calculations. The improved resolution and the direct observation of the crystal field and charge-transfer excitations allow the determination of more accurate parameters than could be derived from X-ray absorption and X-ray photoemission, both limited in resolution by their lifetime broadening. We derive the crystal field and charge-transfer parameters of the Co^{2+} ions, which provides the nature of the ground state of the Co^{2+} ions with respect to symmetry and hybridization. In addition, the increased spectral resolution allows the more accurate determination of the atomic Slater integrals. The results show that the crystal field energy decreases with increasing ligand covalency. The L_2 edge RIXS spectra show that the intensity of the (Coster−Kronig induced) nonresonant X-ray emission is a measure of ligand covalency.

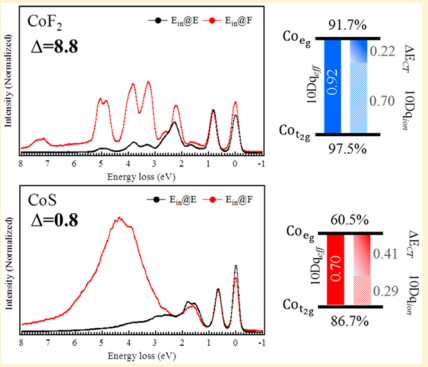

1. INTRODUCTION

The ground-state electronic configuration influences the intrinsic chemical and physical properties of a system, including conductivity, magnetism, and chemical bonds. In the ligand−metal charge-transfer (LMCT) model, the 3d states of a transition-metal ion are assumed to be strongly correlated, where the Co^{2+} ions are approximated with a $3d^7$ ionic configuration. The $3d^7$ configuration is affected by the crystal field interaction, and it interacts with the $3d^8\underline{L}$ configuration via LMCT. The LMCT model has been introduced to classify the 3d transition-metal compounds into different types of insulators or conductors according to values of the Hubbard energy (U) and the LMCT energy (Δ).[1] The electronic structure can be investigated with infrared spectroscopy (IR),[2] optical absorption spectroscopy,[3−6] Raman spectroscopy,[7] and X-ray photoemission spectroscopy (XPS).[8]

2p3d resonant inelastic X-ray scattering (RIXS) is a bulk-sensitive, state- and element-selective measurement able to accurately investigate atomic, crystal field, and charge-transfer information.[9−11] Earlier 2p3d RIXS experiments had energy resolutions in the range of 200−500 meV,[10−16] but this has improved to 30−200 meV in recent years.[17−19] The increased resolution implies that dd-excitations and charge-transfer excitations can be analyzed in more detail.[20] In addition, the low-energy excitations (phonons, magnons) become visible, but this is not analyzed in the present paper. We have chosen cobalt dihalides and CoS as prototype materials to investigate the power of 2p3d RIXS experiments. These systems have been investigated by XPS.[8,21−24] The charge-transfer parameters influence the Neel temperature (T_N) and are correlated with the crystal structure.[25−29] Cobalt chalcogenides are widely used as electrodes of pseudocapacitors,[30,31] hydrogen production catalyst,[32,33] and quantum dot-sensitized solar cells.[34] The understanding of its essential characteristics, such as local atomic structure, oxidation state, or chemical composition, is complicated by various amorphous and nanostructures. Recently, Kornienko et al. used Raman spectroscopy and X-ray absorption spectroscopy (XAS) to investigate the amorphous cobalt sulfide catalysts,[32] but the electronic structure of the cobalt ions were not discussed in detail. We note that, unlike the cobalt dihalides, cobalt sulfides show metallic behavior.[34,35]

In this study, the 2p3d RIXS spectra of CoF_2, $CoCl_2$, $CoBr_2$, and CoS compounds are analyzed systematically using the LMCT model. Although all the crystal structures are different,[25−27] the cobalt ions in these compounds are surrounded by six ligands in an (distorted) octahedral geometry.[21,23] From the

Received: July 13, 2017
Revised: October 27, 2017
Published: October 27, 2017

DOI: 10.1021/acs.jpcc.7b06882
J. Phys. Chem. C 2017, 121, 24919−24928

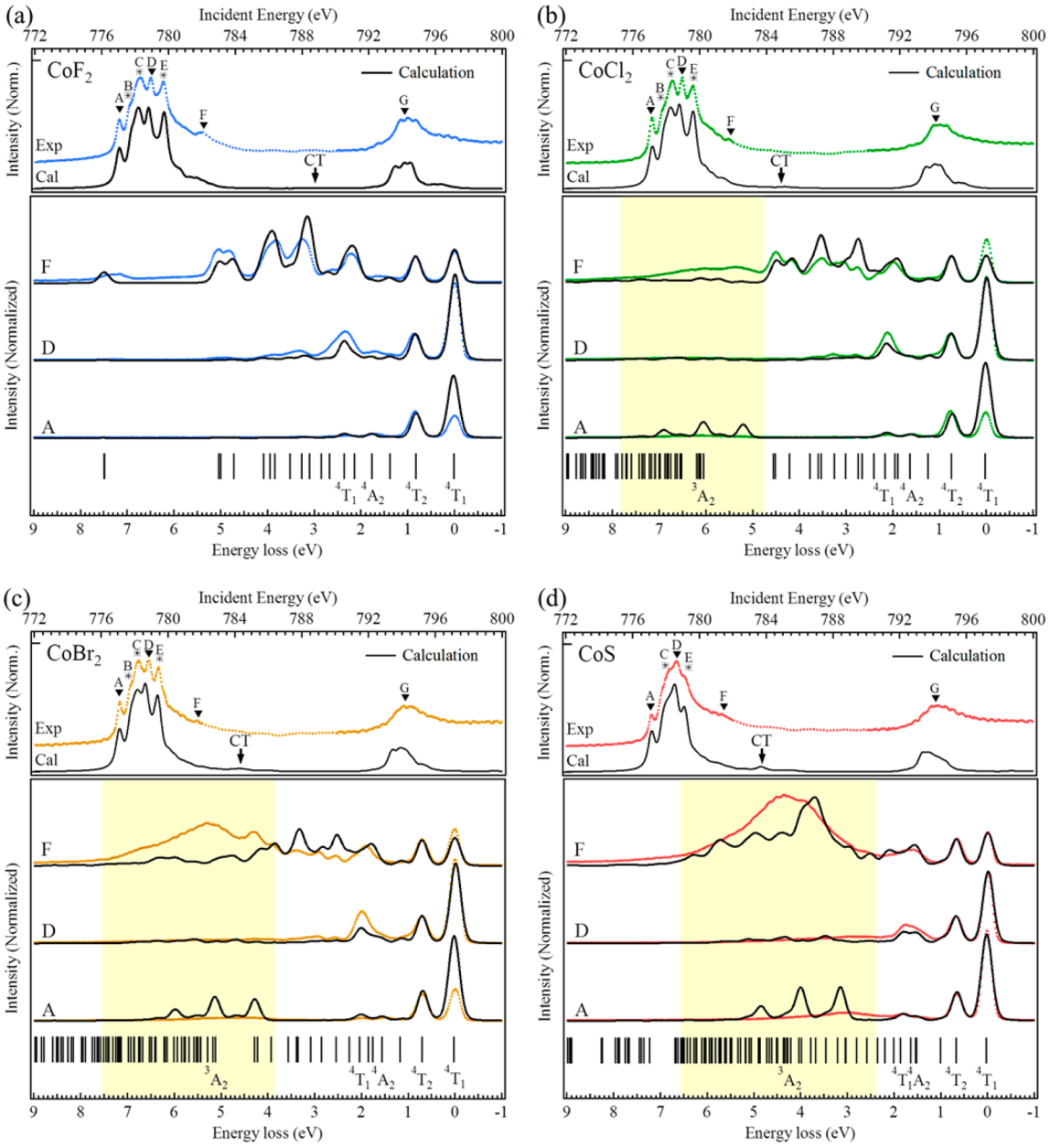

Figure 1. Experimental and simulated 2p XAS (top panels) and the RIXS (bottom panels) spectra of (a) CoF_2, (b) $CoCl_2$, (c) $CoBr_2$, and (d) CoS. The capital labels A−G indicate the incident energies of the RIXS spectra. The yellow blocks indicate the excitation regions of the charge-transfer excitations.

LMCT analysis, we derive relations between covalency, crystal field strength, and peak positions in 2p XAS and 2p3d RIXS.

2. METHODOLOGY

2.1. Experimental Details and Sample Preparation. Cobalt(II) fluoride (powder, >99%, ρ = 4.43 g·cm^{-3}), anhydrous cobalt(II) chloride (beads, −10 mesh, 99.999% trace metals basis, ρ = 3.36 g·cm^{-3}) and anhydrous cobalt(II) bromide (beads, −10 mesh, 99.99% trace metals basis, ρ = 4.91 g·cm^{-3}) were obtained from Sigma-Aldrich. Cobalt sulfide (powder, 99.5%, ρ = 5.45 g·cm^{-3}) was obtained from City Chemical LLC. The powders were applied on carbon tape, attached to the sample holder in an argon atmosphere glovebox, and transferred in an anaerobic environment to the RIXS measurement chamber using a dedicated transfer tool designed for the ADRESS beamline.[36]

XAS and RIXS spectra were measured at the ADRESS beamline of the Swiss Light Source (SLS).[17] The Co $L_{2,3}$ edge (2p) XAS spectra were measured through the drain current and by a photodiode for total electron yield (TEY). The incident energy scale was calibrated measuring the cobalt 2p XAS spectra of the cobalt monoxide powder and comparing it with literature values.[37] The 2p3d RIXS spectra were measured with the use of the high-resolution Super Advanced X-ray Emission Spectrometer (SAXES)[38] of the ADRESS beamline.[17] A scattering geometry was used in which the angle between the incoming light vector and the outgoing one was 90°. The incoming light was polarized in linear parallel mode (linear horizontal; LH) to the scattering plane with a grazing incident angle of 20°. The total resolution of the 2p3d RIXS spectra

DOI: 10.1021/acs.jpcc.7b06882
J. Phys. Chem. C 2017, 121, 24919−24928

were calibrated by measuring the elastic scattering of a noncobalt containing and amorphous reference with the incoming energy from 765 to 785 eV. The combined energy resolution of the RIXS zero-loss peak was found to be 160 meV of full width at half-maximum (fwhm) at the Co L_3 edge (780 eV). The experiments were performed at room temperature and with a pressure below 10^{-9} mbar. The spectra were summed over 6−15 partial spectra that were acquired from 40 to 120 s each (varying to avoid detector saturation). The spot size of the beam was 4×52 μm^2, and the incident flux was estimated as 5×10^{12} ph/s. Using the spectral acquisition times given in Table S1 of the Supporting Information and the freely available Matlab script XASskindose,[39] the skin doses for each CoF_2, $CoCl_2$, $CoBr_2$, and CoS spectrum were estimated to vary between 2.0 and 4.5, 1.9−4.9, 0.9−3.8, and 2.5−7.8 teragray (TGy), respectively. The accumulated skin doses will be three times higher because typically two different sample spots were used to acquire spectra at six excitation energies. Sample integrity was confirmed by repeated measurements of the 2p XAS spectral shape.

2.2. Theory and Simulations. The 2p3d RIXS spectra are calculated with the Kramers−Heisenberg formula:[10,40]

$$I(\omega_i, \omega_f) = \sum_f \left| \sum_m \frac{\langle f|\hat{O}|m\rangle\langle m|\hat{O}|i\rangle}{E_i + \omega_i - E_m - i\frac{\Gamma_m}{2}} \right|^2 \times \delta(E_i + \omega_i - E_f - \omega_f) \quad (1)$$

Here, ω_i and ω_f are the energies of the incident and the emitted photons; E_i, E_f, and E_m are the eigenvalues of the initial state $|i\rangle$, the final state $|f\rangle$, and the intermediate state $|m\rangle$, respectively; Γ_m gives the lifetime broadening of the intermediate state, and $\hat{O}$ is the transition operator, for which the dipole transitions were implied for the case of the 2p3d X-ray absorption and the 3d2p X-ray emission channels. In 2p3d RIXS, $|i\rangle$, $|m\rangle$, and $|f\rangle$ refer to the configurations $2p^63d^n$, $2p^53d^{n+1}$, and $2p^63d^n$, respectively. In addition, if the LMCT hybridization is included, the initial state $|i\rangle$ becomes the linear combination between the ionic configuration ($3d^n$) and configuration with ligand hole ($3d^{n+1}\underline{L}$). By tuning the 2p3d absorption energy, the resonance conditions can emphasize different intermediate states.

Two important phenomena are correlated with the LMCT hybridization within a 3d transition-metal ion: (a) the ligand hybridization influences the metal t_{2g} and e_g states differently;[9] and (b) bonding and antibonding states between original ionic states $|d^n\rangle$ and ligand hole states $|d^{n+1}\underline{L}\rangle$ are created that give rise to the dd-excitations and charge-transfer excitations, respectively.[9,10] These two phenomena will be discussed in terms of (a) the crystal field energy 10Dq and (b) the charge-transfer energy Δ. Using incident energies at various energies of the L_3 edge, it is possible to analyze the details of the dd-excitations and the charge-transfer excitations in the 2p3d RIXS spectra.[9−11] The theoretical details are discussed in section 2 of the Supporting Information.

The beam polarization was defined as LH (LV) as the light was polarized linear parallel (linear perpendicular) to the scattering plane. The experimental 2p3d RIXS spectra were measured with a LH polarization incident beam and a 90° scattering geometry. This experimental setting was simulated as the sum of [LV_{in} to LH_{out}] and [LH_{in} to LV_{out}] polarizations for powder samples. In order to study the 2p XAS and 2p3d RIXS spectral shapes, charge-transfer multiplet (CTM) calculations were used.[9,41,42] A modified version of the code was applied to obtain exact solutions of the charge-transfer Hamiltonian.[43] XAS calculations were performed with CTM4XAS.[44] The charge-transfer RIXS calculations were performed with the use of a dedicated Matlab program.[45] CTM4DOC was used to project the states to their individual basis and to analyze the expansion coefficients in terms of different basis sets.[46]

In a CTM calculation, the following interactions are used: atomic electron−electron interactions, spin−orbit coupling, the crystal field potential, the charge-transfer hybridization, and the broadening parameters. The Slater integrals (F^2_{dd}, F^4_{dd}, F^2_{pd}, G^1_{pd}, and G^3_{pd}) describe the atomic electron−electron interactions in the initial, intermediate, and final states. Alternatively one can use the Racah parameters B and C that are linear combinations of F^2_{dd} and F^4_{dd} ($B = (9\,F^2_{dd} - 5\,F^4_{dd})/441$ and $C = 5\,F^4_{dd}/63$).[47,48] The LMCT effect is included by the single impurity Anderson model,[49,50] considering the interactions between d^n and $d^{n+1}\underline{L}$ configurations, where an electron has been transferred from the ligand valence band while preserving spin and symmetry.[9] The LMCT energy (Δ) is the ionic energy difference between the two configurations, and the electron hopping integrals (T) describe their coupling.[9] The resulting ground-state wave function is a mixture of the d^n and $d^{n+1}\underline{L}$ configurations, which is given as $|\varphi_{GS}\rangle = \alpha\,|d^n\rangle + \beta\,|d^{n+1}\underline{L}\rangle$ with an eigen energy E_{GS}.

3. RESULTS

3.1. 2p3d RIXS Experiments. The top panel in Figure 1 shows the 2p ($L_{2,3}$) XAS spectra of CoF_2, $CoCl_2$, $CoBr_2$, and CoS. All four spectra show the clear signature of a $^4T_1$ high-spin Co^{2+} ground state, equivalent to CoO.[10,51] One can observe that the multiplet states are more and more compressed in the series CoF_2 < $CoCl_2$ ∼ $CoBr_2$ < CoS. To measure the 2p3d RIXS spectra, the incident photon energies were selected in the 2p XAS spectra and labeled with capital symbols A−G (top panels of Figure 1). The chosen incident energies correspond to the different peaks and features of the XAS spectra, as indicated. The incident energies A−F correspond to the $2p_{3/2}$ edge. At the $2p_{1/2}$ edge, only the highest peak energy G was selected for the 2p3d RIXS measurements. In the case of CoS, the multiplet states are compressed, which makes peak B invisible; therefore, no 2p3d RIXS was measured at energy B for CoS.

The bottom panels in Figure 1 present both the experimental and the LMCT-simulated 2p3d RIXS spectra (section 3 of the Supporting Information), where the intensity of the simulation was normalized to the first dd-excitation at approximately 0.7 eV. For CoF_2, a series of sharp features are observable over the whole energy range from 0.0 to 9.0 eV. In fact the peaks continue above 9.0 eV, but the spectra are limited to this energy range to make the low-energy peaks better visible. $CoBr_2$ and CoS also contain the same series of sharp peaks, but they are limited to the range between 0.0 and 3.0 eV. Between 3.0 and 7.0 eV, broader features are visible. The 2p3d RIXS final states relate to excitations of the $^4T_1$ Co^{2+} ions. One can make a direct comparison to optical spectroscopy and relate the sharp peaks with dd-excitations and the broad peaks with charge-transfer excitations. A difference with optical spectroscopy is that the dd-excitations are dipole-forbidden in direct optical absorption, which makes them weak in intensity.[3−6] Because 2p3d RIXS is a dipole excitation plus dipole decay transition, the dd-excitations are strong. In fact, for CoF_2 and $CoCl_2$ the dd-excitations are stronger than the charge-transfer excitations. Experimentally we conclude that in 2p3d RIXS we reach equivalent final states as in optical absorption with an inverted

DOI: 10.1021/acs.jpcc.7b06882
J. Phys. Chem. C 2017, 121, 24919−24928

Table 1. Slater Integral and Spin−Orbit Coupling Energies in the Simulation (in eV)[a]

	F^2_{dd}	F^4_{dd}	F^2_{pd}	G^1_{pd}	G^3_{pd}	ζ_p	ζ_d
$2p^63d^7$	9.470	6.805	–	–	–	–	0.066
$2p^63d^8\underline{L}$	8.512	6.072	–	–	–	–	0.059
$2p^53d^8$	10.115	7.276	6.389	4.318	2.701	9.748	0.083
$2p^53d^9\underline{L}$	–	–	5.83	3.895	2.435	9.750	0.075

[a]The slater integrals values F^2_{dd}, F^4_{dd}, F^2_{pd}, G^1_{pd}, and G^3_{pd} are 82%, 94%, 88%, 80%, and 88% of the Hartree−Fock values, respectively.

intensity strength where dd-excitations are stronger than charge-transfer excitations.

3.2. 2p3d RIXS Simulations. The spectral features are calculated with the Kramers−Heisenberg equation using the incident photon energies from the experiments. The general procedure in the 2p3d RIXS calculations is the following:

(1) We calculate the atomic parameters for the Co^{2+} ion, using the common approach in CTM4XAS of using 80% of the Hartree−Fock calculated values for the Slater integrals plus the spin−orbit couplings as calculated for the free ion.
(2) We use the 2p3d RIXS spectra of each compound to determine the value of 10Dq.
(3) We use the 2d3p RIXS spectra of each compound to determine Δ.
(4) Keeping the optimized 10Dq and Δ, the atomic parameters were optimized to obtain the best fit for both the 2p XAS and all 2p3d RIXS spectra, where the same parameters are used for all four systems.

First we describe the comparison with the 2p3d RIXS experiments. In section 3.3 we describe the procedure to determine the value of 10Dq. In section 3.4 we describe the procedure to determine the value of Δ and the consequence of charge transfer on the crystal field splitting.

All CTM calculations were performed in C_4 symmetry at 300 K using a small exchange field ($M \sim 2$ meV) to take the antiferromagnetic order ($T_N \sim 10$−40 K) into account.[27−29] The 300 K results were calculated by considering the first six energy states and summing them with a Boltzmann distribution weighting. Because of the contraction of the 3d wave function due to the core hole, the 10Dq value is reduced with 15% for the intermediate state.[52] The charge-transfer parameters include the charge-transfer energy Δ, the Hubbard Coulomb repulsion between the 3d electrons U_{dd} (U), the core hole potential U_{pd} (Q), and the electron hopping parameters T. In this article, the parameters were fixed by using $U = 6$ eV, $Q = 7$ eV, $T_{t_{2g}} = 1$ eV, and $T_{e_g} = 2$ eV. Note that 2p XAS and 2p3d RIXS are not sensitive to the values of U and Q, but only to their energy difference. For Co^{2+}, only $3d^7$ and $3d^8\underline{L}$ configurations were considered in the calculations. The $3d^9\underline{L}^2$ and $3d^{10}\underline{L}^3$ configurations were neglected when reproducing the 2p XAS and the 2p3d RIXS spectral shapes.[53]

As described above, the initial calculations were performed with atomic Slater integrals, defined as 80% of their Hartree−Fock value. 2p3d RIXS allows for a refinement of the atomic parameters: The combination of (a) its 160 meV resolution, (b) the multiple resonant spectra, and (c) the large number of spectral features allows for a further refinement of the atomic interactions. The optimized values of the Slater integrals are given in Table 1 (see section 4d of the Supporting Information), where we note that in O_h symmetry the exchange interaction for e_g and t_{2g} states is not exactly the same.[54] The F^2_{dd} and F^4_{dd} are not necessarily reduced by the similar reduction values. The lifetime of the 2p core states is approximately constant for the L_3 edge.[55,56] The lifetime broadening (L) of the 2p core hole was set to 0.4 eV fwhm,[10,57] and we add the experimental resolution with a Gaussian value of 0.16 eV fwhm. The final states of 2p3d RIXS relate to dd-excitations that are known from optical spectroscopy.[3−6] The lifetime of the dd-excitations varies depending on the spin state. We use a broadening of 50 meV fwhm for lifetime of dd-excitations and the Gaussian broadening of 160 meV for simulating both incoming and outgoing beams. Because the elastic $^4T_1$ peak is split into 12 individual states spread over 100 meV,[51] its overall broadening is ∼250 meV.

We analyzed the nature of the lowest-lying states of $3d^7$ configuration that are given with their $^4T_1$, $^4T_2$, and $^4A_2$ Mulliken symbols in Figure 1 and listed in Table 2. The yellow block indicates the region of the charge-transfer excitations, where a large charge-transfer energy Δ shifts them to higher excitation energies. The charge-transfer peaks provide a determination for the hybridization information and will be further discussed in section 3.4. In general, the energy and shape of the excitations are well-reproduced, especially in the first 2 eV. The peaks at higher excitation energies above 3.0 eV were not simulated as accurately, which is related to the approximations to the $3d^8\underline{L}$ charge-transfer band due to limitations in computer power. The full charge-transfer band has been approximated with three charge-transfer states that yield features that are too sharp at energies above 3.0 eV.

Table 2. RIXS-Derived State Symmetry Term Symbols and Energies (in eV) and Their Comparison to Calculations

	CoF_2	$CoCl_2$	$CoBr_2$	CoS
	exptl/calcd	exptl/calcd	exptl/calcd	exptl/calcd
		Quartet		
$^4T_1$	0.00/0.00	0.00/0.00	0.00/0.00	0.00/0.00
$^4T_2$	0.85/0.81	0.77/0.72	0.71/0.68	0.67/0.65
$^4A_2$	1.71/1.76	1.60/1.61	1.52/1.54	1.44/1.51
$^4T_1$	2.27/2.35	2.11/2.14	1.98/2.02	1.79/1.83
		Charge Transfer		
$^3A_2$ (CT)	11.50/11.26	6.12/6.11	5.30/5.30	3.94/4.20

With Figure 2 we emphasize the excitation selectivity. At incident energies A−E, the 0−2 eV excitations dominate, but at incident energy F, more intensity is found at the higher excitation energies. In the case of CoF_2, the spectra at energy F gives dd-excitations in the whole energy loss region between 0 and 8 eV (Figure 2a). The spectra at energy F of CoS shows a large and broad feature at about 4 eV (Figure 2b) that can be assigned to charge-transfer excitations.

3.3. Determination of the Crystal Field Value 10Dq from 2p3d RIXS Experiments. In our CTM simulation, 10Dq and Δ are the only two free parameters that are used in addition to the fixed atomic parameters. From the Tanabe−Sugano diagram[3] it is known that the effective value of 10Dq is

DOI: 10.1021/acs.jpcc.7b06882
J. Phys. Chem. C 2017, 121, 24919−24928

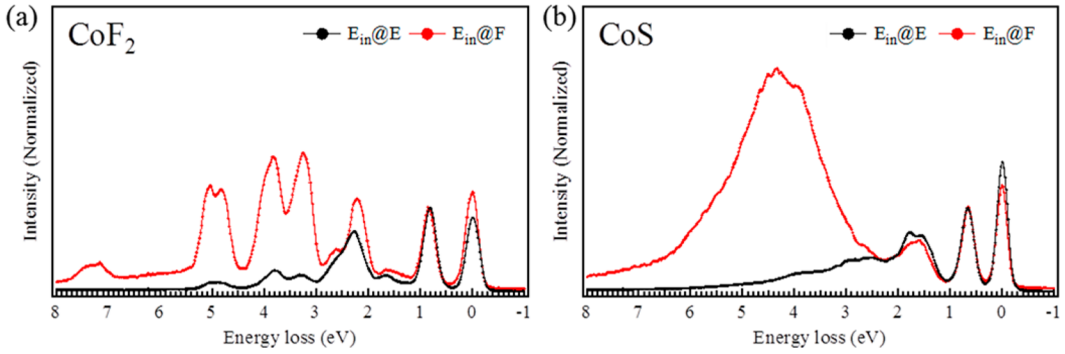

Figure 2. Experimental results at incident energies E and F of (a) CoF_2 and (b) CoS.

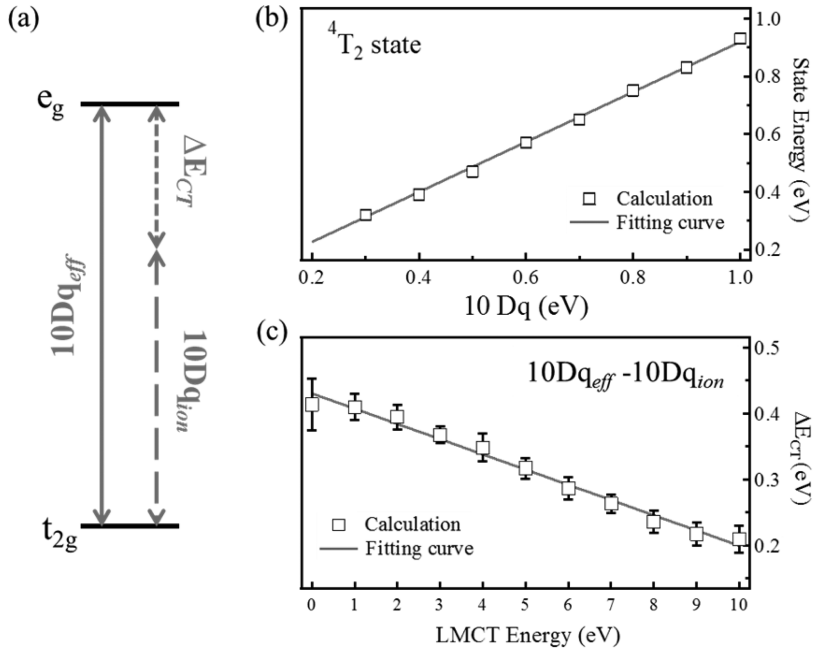

Figure 3. (a) Conceptual contributions of $10Dq_{eff}$. (b) Energy difference between the ground state ($^4T_1$) and the first dd-excitation ($^4T_2$) as a function of 10Dq without LMCT effect. (c) ΔE_{CT} correlation with respect to LMCT energy Δ. The fitted straight lines in panels b and c provide the values given in eqs 2 and 3, respectively. The error in panel c is the error of different calculation sets to the their average point (details in section 4c of the Supporting Information).

close to the splitting between the ground state and the first dd-excitations. In other words, the first peak in the dd-excitations will be close to the value of 10Dq. We will investigate the relation between the first dd-excitation energy and 10Dq. In the Co^{2+} ($3d^7$) high-spin Tanabe–Sugano diagram (Figure S5), the energy difference between the $^4T_1$ and $^4T_2$ states is linear in 10Dq between 0.2 and 1 eV. This energy difference corresponds to the first dd-excitation in the 2p3d RIXS spectra. As such, one can track the 10Dq value by locating the first dd-excitation peak, which is more reliable than fitting the 2p XAS spectrum.[53] The energy difference between the $^4T_1$ and $^4T_2$ sates has been collected in Figure 3b. From these data points, the following relation regarding the crystal field splitting was derived (see section 4 of the Supporting Information for more details):

$$\Delta E_{^4T_1-^4T_2} = 0.865 \times 10Dq + 0.0534 \quad (2)$$

This equation shows that the difference between $^4T_1$ and $^4T_2$ states is not exactly equal to 10Dq, but they are correlated with a linear relationship. From this relation we can determine the 10Dq value experimentally from the first dd-excitation of the 2p3d RIXS spectra. The peak maxima of the first dd-excitations are 0.85, 0.77, 0.71, and 0.67 eV for CoF_2, $CoCl_2$, $CoBr_2$, and CoS, respectively (the $^4T_2$ state in Figure 4a). In all cases the first peak relates to the $^4T_2$ state.[3−7,10,51] The 10Dq values of the compounds were converted using eq 2, and they are 0.92, 0.81, 0.75, and 0.70 eV for CoF_2, $CoCl_2$, $CoBr_2$, and CoS, respectively. This relates to an increase with respect to first dd-excitation by 0.07, 0.04, 0.04, and 0.03 eV, respectively.

3.4. Ionic and Covalent Contribution to the Crystal Field Splitting. When the LMCT effect is considered, the charge transfer contributes to the e_g–t_{2g} splitting, i.e., the overall effective crystal field is caused by both ionic and charge-transfer contributions. The total crystal field splitting ($10Dq_{eff}$) should be reconsidered as the effect from two components:

1. The ionic crystal field value ($10Dq_{ion}$)
2. The charge-transfer contribution (ΔE_{CT})

Figure 3a shows the ionic and charge-transfer contributions of the crystal field splitting. In the simulations we relate the first dd-peak to the total crystal field splitting, which implies that after the determination of the charge-transfer energy Δ, we

DOI: 10.1021/acs.jpcc.7b06882
J. Phys. Chem. C 2017, 121, 24919−24928

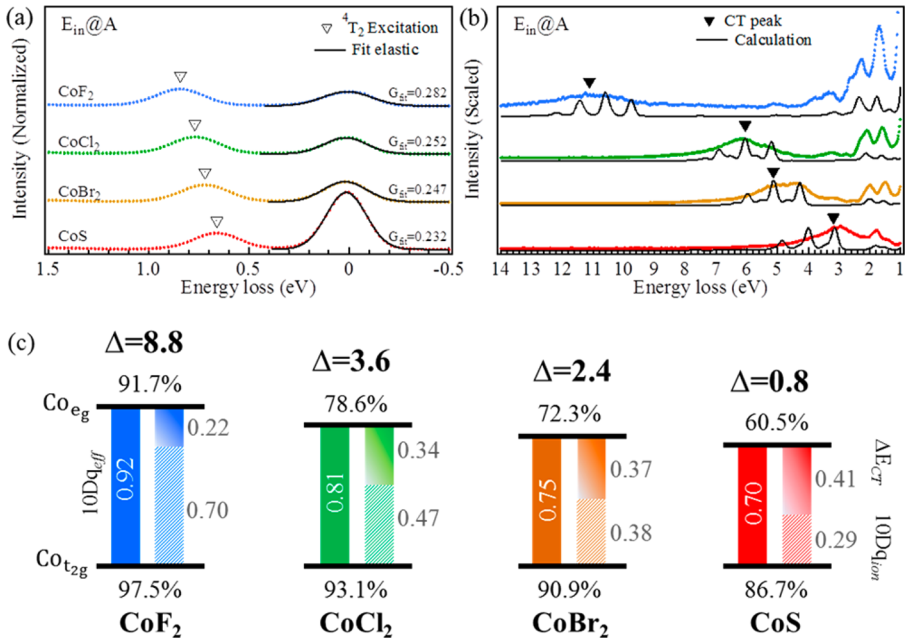

Figure 4. Zoom of the 2p3d RIXS spectra at incident energy A in (a) the low-energy loss region (between −0.5 and 2 eV) and (b) the charge-transfer excitation region. (c) Graphical representation of the conceptual effective crystal field energy splitting and the cobalt ionic orbital covalence in a function of Δ.

have to adjust $10Dq_{ion}$. Figure 3c shows the results for a series of calculations as a function of Δ. One can observe a linear trend between the value of Δ and ($10Dq_{eff} - 10Dq_{ion}$). This implies that there is a linear relation between the charge-transfer contribution (ΔE_{CT}) and Δ (cf. Figure 3c):

$$\Delta E_{CT} = 10Dq_{eff} - 10Dq_{ion} \sim 0.43 - 0.0239 \times \Delta \quad (3)$$

We optimized the Δ values by comparing the calculated charge-transfer peak to the experimental spectra. In Table 3 the Δ and ΔE_{CT} values are given, and after eq 3 was applied, the ionic crystal energy $10Dq_{ion}$ was obtained. Figure 4c summaries the contributions of $10Dq_{eff}$ (filled bars), $10Dq_{ion}$ (striped bars), and ΔE_{CT} (slide bars) in a graphical presentation.

Table 3. Experimental First dd-Excitation and its Relation to Different 10Dq Values and Δ

	first dd	$10Dq_{eff}$	$10Dq_{ion}$	ΔE_{CT}	Δ
CoF_2	0.85	0.92	0.70	0.22	8.8
$CoCl_2$	0.77	0.81	0.47	0.34	3.6
$CoBr_2$	0.71	0.75	0.38	0.37	2.4
CoS	0.67	0.70	0.29	0.41	0.8

4. DISCUSSION

4.1. Width of the Elastic Peak. An interesting observation is that the width of the elastic peak in CoF_2 (fwhm ∼280 meV) is larger than that in CoS (fwhm 230 meV), whereas the experiment resolution was 160 meV with an uncertainty of less than 10 meV. In other words, the observed elastic peak broadenings are larger than the experiment resolution. This implies that there are additional broadening mechanisms due to (1) 3d spin−orbit coupling, (2) magnetic exchange, (3) symmetry distortions, and/or (4) vibrations. The effects 1−3 split the $^4T_1$ ground state.[51] Infrared spectroscopy results[2] show that the highest energy of the spin−orbit coupling peak (interacting with the exchange field) is 0.173 eV for CoF_2, while the energies for $CoCl_2$ and $CoBr_2$ are 0.148 and 0.143 eV, respectively, confirming the 0.03 eV broadening difference in Figure 4a. One possible reason for this effect is that when the Δ value is smaller, the d^n and $d^{n+1}\underline{L}$ configurations are more hybridized, leading to an effective reduction of the 3d spin−orbit coupling. An alternative scenario is that the more ionic the compound, the larger the effect of a crystal field distortion.

4.2. Ground-State Analysis and Differential Orbital Covalency. The LMCT energies listed in Table 3 were determined according to the charge-transfer excitations as emphasized in Figure 4b. A trend of the charge-transfer excitations is visible as a function of Δ. The obtained Δ values were 8.8, 3.6, 2.4, and 0.8 eV with respect to the CoF_2, $CoCl_2$, $CoBr_2$, and CoS samples. The center of the features were extracted from the spectra and are given in Table 2. A smaller Δ value leads to a stronger hybridization of ground state between the $3d^7$ and $3d^8\underline{L}$ configurations, in which the ground state can

Table 4. Orbital Occupation and Covalency Analysis of CoF_2, $CoCl_2$, $CoBr_2$, and CoS

	$\|d^7\rangle$		$\|d^8\underline{L}\rangle$			metal covalency			
	$\|t_2^5e^2\rangle$	$\|t_2^4e^3\rangle$	$\|t_2^5e^3\underline{L}\rangle$	$\|t_2^6e^2\underline{L}\rangle$	$\|t_2^4e^4\underline{L}\rangle$	T_{2g}	E_g	DOC	$\langle n\rangle$
CoF_2	85.3	8.6	5.1	0.8	0.3	97.5	91.7	5.8	7.06
$CoCl_2$	75.7	8.3	12.9	2.1	1.0	93.1	78.6	14.4	7.16
$CoBr_2$	71.0	8.1	16.7	2.7	1.4	90.9	72.3	18.6	7.21
CoS	62.5	7.4	23.8	4.0	2.3	86.7	60.5	26.2	7.30

DOI: 10.1021/acs.jpcc.7b06882
J. Phys. Chem. C 2017, 121, 24919−24928

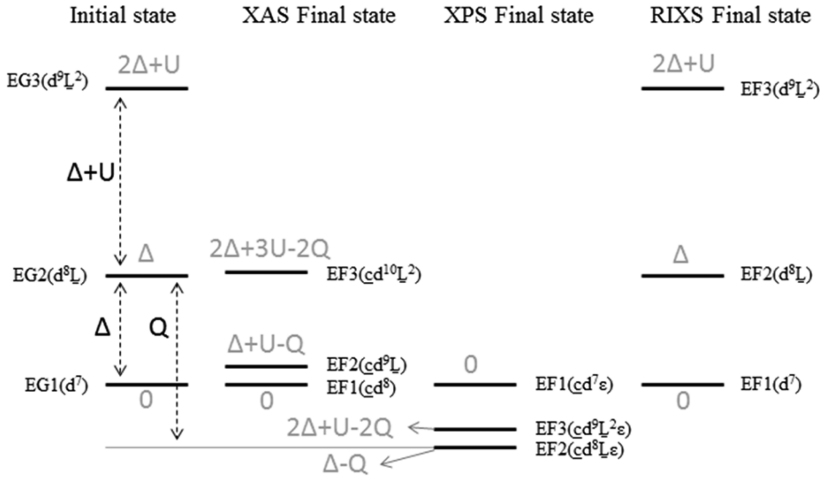

Figure 5. Initial ground and final state energy configurations of XAS, XPS, and RIXS.

be described by $|\varphi_{GS}\rangle = \alpha|3d^7\rangle + \beta|3d^8\underline{L}\rangle$ with the population coefficient values α and β. This gives the hybridization percentages of the original multiplet ($|\alpha|^2$) and the ligand hole multiplet configuration ($|\beta|^2$).

To obtain the hybridization percentages, the microstates of the ground state are projected into separate $3d^7$ and $3d^8\underline{L}$ configurations of specific orbitals derived from symmetry (in octahedral symmetry, for example, in terms of e_g and t_{2g} orbitals).[46] The results are shown in Table 4. It is observed therein that the percentage of the $|3d^7\rangle$ states on the cobalt ion decreases with decreasing Δ. The percentage of ligand-hybridized $|3d^8\underline{L}\rangle$ states for CoS is ∼30%. From these numbers, the metal covalency of the e_g and t_{2g} orbitals can be estimated. Here we consider only one-electron hopping from the ligand to the metal ion e_g or t_{2g} orbitals. Hence, only the $3d^7$ ground state $|t_{2g}^5e_g^2\rangle$ and the ligand hole e_g $|t_{2g}^5e_g^3\underline{L}\rangle$ and t_{2g} $|t_{2g}^6e_g^2\underline{L}\rangle$ states are taken into account. The covalence fraction of cobalt within e_g orbitals is then given by

$$C(e_g) = 100\% - \frac{3}{2} \times \left(\frac{P_{t_{2g}^5e_g^3}}{P_{t_{2g}^5e_g^2} + P_{t_{2g}^5e_g^3\underline{L}} + P_{t_{2g}^6e_g^2\underline{L}}} \right) \quad (4)$$

where $\frac{3}{2}$ is a renormalization factor (2 out of 3 holes in the d^7 configuration are in e_g orbitals) and $P_{t_{2g}^xe_g^y}$ are the percentages for configuration $t_{2g}^xe_g^y$ as given in Table 4. This implies that the covalence fraction of cobalt within the e_g orbitals is reduced from 100% by the corresponding fraction of ligand character within these e_g orbitals. Similarly, the covalence fraction of cobalt in the t_{2g} orbitals is then given by

$$C(t_{2g}) = 100\% - \frac{3}{1} \times \left(\frac{P_{t_{2g}^6e_g^2}}{P_{t_{2g}^5e_g^2} + P_{t_{2g}^5e_g^3\underline{L}} + P_{t_{2g}^6e_g^2\underline{L}}} \right) \quad (5)$$

It follows that, when going through the series from CoF_2 to CoS, the cobalt ion character in the e_g orbitals decreases faster than that in the t_{2g} orbitals (Figure 4c). In octahedral symmetry, the ligand 2p orbitals overlap strongly with the cobalt 3d e_g ($d_{x^2-y^2}$ and d_{z^2}) orbitals; thus, ligand hybridization is affecting e_g orbitals more than t_{2g} orbitals. By subtracting the e_g from the t_{2g} orbital covalency one obtains the differential orbital covalency (DOC)[58] as given in Table 4. The DOC values are dependent on crystal field symmetry and strength, as well as charge-transfer hopping energies. Note that we obtain a similar DOC value for CoS as obtained for $[FeCl_6]^{3-}$ with similar symmetry and charge-transfer settings:[58] CoS (Δ = 0.8 eV; T_{e_g}:$T_{t_{2g}}$ = 2:1) and $[FeCl_6]^{3-}$ (Δ = 0.1 eV; T_{e_g}:$T_{t_{2g}}$ ∼ 2:1) have DOC values of 25−27%.

4.3. Charge-Transfer Parameters Derived from 2p3d RIXS Compared with 2p XPS. When the Δ values in Table 2 are compared with XPS-derived Δ values,[8] only the value for CoF_2 is found to be equal (RIXS, 8.8 eV vs XPS, 8.6 eV). $CoCl_2$ (RIXS, 3.6 eV vs XPS, 4.5 eV) and $CoBr_2$ (RIXS, 2.4 eV vs XPS, 3.5 eV) show less agreement. For CoS, a small Δ value (0.8 eV) was found, which is related to the sample exhibiting metallic behavior.[1,34] First, a simulation including the third configuration $3d^9\underline{L}^2$ has been tested (Figure S11). In the case of $CoBr_2$, the three-configuration calculation shifts the charge-transfer excitation ∼0.3 eV lower than the two-configuration calculation with the same Δ value. In other words, the Δ value should be ∼2.7 eV (2.4 + 0.3) for $CoBr_2$ when we consider the third configuration. This brings the Δ value a bit closer to, but smaller than, the XPS value (3.5 eV).

Figure 5 displays the final state configurations of the XAS, XPS, and RIXS processes. It shows the energy differences between the ionic configuration and the two charge-transfer configurations. The notations EG and EF refer to ground and final states, respectively. The numbers 1, 2, and 3 refer to configurations with zero, one, and two ligand hole(s), respectively. The charge-transfer configurations show that the core−hole potential (Q) needs to be taken into account in the case of XAS and XPS spectra. This implies that we have to optimize Q (in addition to Δ) to simulate the XAS and XPS spectra. Because of the larger screening effects, at least three charge-transfer configurations need to be taken into account for XPS spectra.[21,59] On the other hand, the relative final state energy of the first LMCT configuration in valence RIXS is Δ. Being independent of Q, the core−hole will not contribute to the relative configuration energy in 2p3d RIXS, where we note that via its influence on 2p XAS Q could influence the intensities. We ignore the second LMCT configuration in the RIXS calculations. As indicated in Figure 5, the relative initial and final state energies of the second LMCT configuration are $2\Delta + U$ in RIXS. In the vast majority of cases, its relative energy will be significantly higher than that of the first LMCT configuration and will play a negligible role in the spectral shape. Finally, we note that our Δ and $10Dq_{ion}$ determinations

DOI: 10.1021/acs.jpcc.7b06882
J. Phys. Chem. C 2017, 121, 24919−24928

are in line with CTM analysis of CoO 2p3d RIXS by Magnuson et al.[10]

We conclude that RIXS is more accurate for the determination of Δ due to (1) the sharper experimental features and (2) the smaller (nonlocal) screening effects. Note that the uncertainty in the atomic parameters (and in 10Dq) is also present in XPS, but because of the absence of spectral features it is not possible to gain experimental information regarding their exact values. Because 2p XAS and 2p3d RIXS are not sensitive to the separate values of *U* and *Q*, a full electronic structure determination would ideally consist of 2p3d RIXS combined with 2p XPS, or another (resonant) photoemission/Auger experiment.

4.4. Use of the Coster–Kronig Auger Channel to Determine the Covalency. In this section, the L_2 ($2p_{1/2}3d$) edge RIXS spectra are discussed. In comparison with the L_3 ($2p_{3/2}3d$) edge RIXS spectra, the L_2 edge RIXS spectra give the resonant spectra of L_2 ($3d2p_{1/2}$) emission and in addition the nonresonant spectra of L_3 ($3d2p_{3/2}$) emission. Figure 6 shows

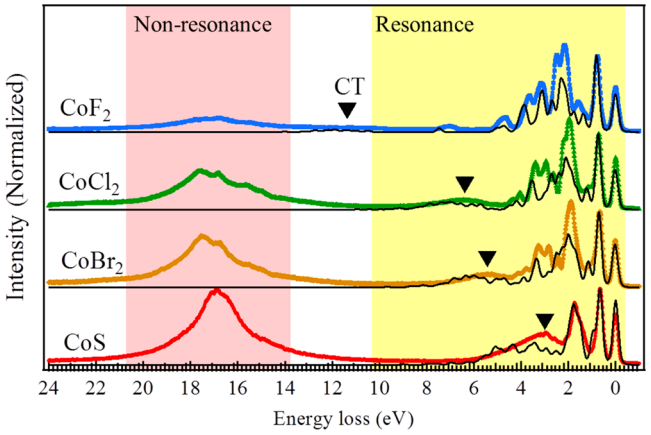

Figure 6. Experimental (colored traces) and simulated (black lines) RIXS spectra at incident energy G.

the experimental and calculated results. Between 0 and 10 eV the spectra show the dd-excitations and the charge-transfer excitations, reproduced with the same procedure as discussed above. New features were observed in the high energy loss region. These features relate to X-ray emission from the $3d2p_{3/2}$ channel. The integrated intensity ratio between nonresonant (9–25 eV) and resonant (−2 to 8.5 eV) emissions (L_3/L_2) are ∼0.55, 1.06, 1.22, and 1.71 for CoF_2, $CoCl_2$, $CoBr_2$, and CoS, respectively.

In order to explain these features, the core hole decay was simplified in two groups: radiative decay (X-ray emission) and nonradiative or electronic decay (Auger). In the case of 2p core holes in 3d transition-metal ions, the electronic decay channels constitute more than 99% of the total decay, and they dominate the lifetime.[11,20,56] These Auger channels are dominated by the 2p3p3p, 2p3p3d, and 2p3d3d decays. In the resonant $2p_{1/2}3d$ X-ray emission, the RIXS signal follows the process

$$2p^2_{1/2}2p^4_{3/2}3d^7 \xrightarrow{L_2\ \text{absorption}} 2p^1_{1/2}2p^4_{3/2}3d^8$$
$$\xrightarrow{L_2\ \text{emission}} 2p^2_{1/2}2p^4_{3/2}3d^7$$

The scattering cross section is proportional to the radiative decay. In the case of the nonresonant channel, a Coster–Kronig Auger channel is involved in the first step of the decay process:[20]

$$2p^2_{1/2}2p^4_{3/2}3d^7 \xrightarrow{L_2\ \text{absorption}} 2p^1_{1/2}2p^4_{3/2}3d^8$$
$$\xrightarrow{\text{CK auger}} 2p^2_{1/2}2p^3_{3/2}3d^8 \xrightarrow{L_3\ \text{emission}} 2p^2_{1/2}2p^4_{3/2}3d^7$$

The $3d2p_{3/2}$ X-ray emission intensity is proportional to the strength of the Coster–Kronig Auger channel, where the other Auger channels are equivalent in strength for the L_3 and the L_2 edges.[18,49,55] The large L_3 X-ray emission for CoS implies that the Coster–Kronig channel is strong, which is correlated with the large charge-transfer effects. This behavior has also been studied on cobalt clusters in SiO_2[49] and iron-based superconductors.[60−62] Our conclusion is that the intensity of the Coster–Kronig induced nonresonant X-ray emission is a measure of the covalency of a system, where further study is required to quantify this effect for different elements.

5. CONCLUSIONS

We have measured high-resolution 2p3d RIXS results of CoF_2, $CoCl_2$, $CoBr_2$, and CoS. Charge-transfer multiplet calculations are able to accurately reproduce the spectral shapes. The analysis revealed accurate values of the charge-transfer energy Δ and the crystal field value 10Dq, where the crystal field is split into ionic and charge-transfer contributions. In comparison with XPS, 2p3d RIXS is a more accurate method to determine the charge-transfer energy (Δ). In addition, it is more precise regarding the crystal field value 10Dq and also in determining the atomic electron–electron interactions (Slater integrals).

From the simulations, the orbital occupancies of the different states are given, and the corresponding differential orbital covalency analysis confirms that CoS is significantly more covalent than CoF_2. It is observed experimentally that the broadening of the quasi-elastic peak become gradually smaller while going from ionic CoF_2 to covalent CoS, due to either an effective reduced 3d spin–orbit coupling and/or symmetry distortions.

The L_2 edge RIXS spectra are analyzed with respect to the integrated intensity ratio between resonant ($2p_{1/2}3d$) and nonresonant ($2p_{3/2}3d$) X-ray emissions, which are ∼0.55, ∼1.06, ∼1.22, and ∼1.71 for CoF_2, $CoCl_2$, $CoBr_2$, and CoS, respectively. These numbers show that the Coster–Kronig channel is stronger in CoS, and we conclude that the ratio between resonant and nonresonant decay is a potential tool to probe the effects of electron delocalization.

■ ASSOCIATED CONTENT

Supporting Information

The Supporting Information is available free of charge on the ACS Publications website at DOI: 10.1021/acs.jpcc.7b06882.

Applied X-ray skin doses, charge-transfer multiplet calculation and single-impurity Anderson model, details on the experimental and simulated results, Tanabe–Sugano diagrams and the effects of charge transfer (PDF)

■ AUTHOR INFORMATION

Corresponding Authors

*E-mail: M.M.vanschooneveld@gmail.com. Tel: (+31) 302537400.

*E-mail: F.M.F.deGroot@uu.nl. Tel: (+31) 302537400.

DOI: 10.1021/acs.jpcc.7b06882
J. Phys. Chem. C 2017, 121, 24919−24928

ORCID

Ru-Pan Wang: 0000-0003-4495-9881

Frank M. F. de Groot: 0000-0002-1340-2186

Notes

The authors declare no competing financial interest.

■ ACKNOWLEDGMENTS

Experiments have been performed at the ADRESS beamline of the Swiss Light Source at the Paul Scherrer Institut, Villigen, Switzerland. We thank C. Monney for his assistance during the measurements. Financial support was provided through Rubicon Grant 680-50-1206 of The Netherlands Organization for Scientific Research (NWO) and the ERC advanced grant XRAYonACTIVE, Number 340279.

■ REFERENCES

(1) Zaanen, J.; Sawatzky, G. A.; Allen, J. W. Band Gaps and Electronic Structure of Transition-metal Compounds. *Phys. Rev. Lett.* **1985**, *55*, 418−421.

(2) Newman, R.; Chrenko, R. M. Infrared Absorption from L·S Splittings in Co^{2+} Salts. *Phys. Rev.* **1959**, *115*, 1147−1152.

(3) Tanabe, Y.; Sugano, S. On the Absorption Spectra of Complex Ions II. *J. Phys. Soc. Jpn.* **1954**, *9*, 766−779.

(4) Ferguson, J.; Wood, D. L.; Knox, K. Crystal-field Spectra of d^3, d^7 Ions. II. $KCoF_3$, $CoCl_2$, $CoBr_2$, and $CoWO_4$. *J. Chem. Phys.* **1963**, *39*, 881−889.

(5) Zimring, L. J.; Stout, J. W. Polarized Crystal Spectra of CoF_2 and $Co_{0.06}Zn_{0.94}F_2$. *J. Chem. Phys.* **1969**, *51*, 4197−4209.

(6) Blunt, R. F. Optical Absorption of Cobalt in Manganese Fluoride. *J. Chem. Phys.* **1966**, *44*, 2317−2320.

(7) Lockwood, D. J.; Mischler, G.; Johnstone, I. W.; Schmidt, M. C. Raman Scattering from Electronic Excitations and Phonons in Paramagnetic and Antiferromagnetic $CoBr_2$. *J. Phys. C: Solid State Phys.* **1979**, *12*, 1955−1975.

(8) Kinsinger, V.; Zimmermann, R.; Hüfner, S.; Steiner, P. Core Level Exchange Splittings in Transition Metal Compounds. *Z. Phys. B: Condens. Matter* **1992**, *89*, 21−27.

(9) de Groot, F. M. F. Multiplet Effects in X-ray Spectroscopy. *Coord. Chem. Rev.* **2005**, *249*, 31−63.

(10) Magnuson, M.; Butorin, S. M.; Guo, J.-H.; Nordgren, J. Electronic Structure Investigation of CoO by Means of Soft X-ray Scattering. *Phys. Rev. B: Condens. Matter Mater. Phys.* **2002**, *65*, 205106.

(11) Butorin, S. M.; Guo, J.-H.; Magnuson, M.; Nordgren, J. Resonant Inelastic Soft X-ray Scattering from Valence-band Excitations in $3d^0$ Compounds. *Phys. Rev. B: Condens. Matter Mater. Phys.* **1997**, *55*, 4242−4249.

(12) Jiménez-Mier, J.; Herrera-Pérez, G. M.; Olalde-Velasco, P.; Ederer, D. L.; Schuler, T. Ligand Field and Interference Effects in L-edge X-ray Raman Scattering of MnF_2 and CoF_2. *Rev. Mex. Fis.* **2008**, *54*, 30−35.

(13) Butorin, S. M.; Mancini, D. C.; Guo, J.-H.; Wassdahl, N.; Nordgren, J.; Nakazawa, M.; Tanaka, S.; Uozumi, T.; Kotani, A.; Ma, Y.; et al. Resonant X-ray Fluorescence Spectroscopy of Correlated Systems: A Probe of Charge-transfer Excitations. *Phys. Rev. Lett.* **1996**, *77*, 574−577.

(14) Ghiringhelli, G.; Matsubara, M.; Dallera, C.; Fracassi, F.; Gusmeroli, R.; Piazzalunga, A.; Tagliaferri, A.; Brookes, N. B.; Kotani, A.; Braicovich, L. NiO as a Test Case for High Resolution Resonant Inelastic Soft X-ray Scattering. *J. Phys.: Condens. Matter* **2005**, *17*, 5397−5412.

(15) Kotani, A.; Matsubara, M.; Uozumi, T.; Ghiringhelli, G.; Fracassi, F.; Dallera, C.; Tagliaferri, A.; Brookes, N. B.; Braicovich, L. Theoretical and Experimental Study of Resonant Inelastic X-ray Scattering for NiO. *Radiat. Phys. Chem.* **2006**, *75*, 1670−1675.

(16) Matsubara, M.; Uozumi, T.; Kotani, A.; Parlebas, J. C. Charge Transfer Excitation in Resonant X-ray Emission Spectroscopy of NiO. *J. Phys. Soc. Jpn.* **2005**, *74*, 2052−2060.

(17) Strocov, V. N.; Schmitt, T.; Flechsig, U.; Schmidt, T.; Imhof, A.; Chen, Q.; Raabe, J.; Betemps, R.; Zimoch, D.; Krempasky, J.; et al. High-Resolution Soft X-ray Beamline ADRESS at the Swiss Light Source for Resonant Inelastic X-ray Scattering and Angle-Resolved Photoelectron Spectroscopies. *J. Synchrotron Radiat.* **2010**, *17*, 631−643.

(18) Ghiringhelli, G.; Piazzalunga, A.; Wang, X.; Bendounan, A.; Berger, H.; Bottegoni, F.; Christensen, N.; Dallera, C.; Grioni, M.; Grivel, J.-C.; et al. Crystal Field and Low Energy Excitations Measured by High Resolution RIXS at the L_3 Edge of Cu, Ni and Mn. *Eur. Phys. J.: Spec. Top.* **2009**, *169*, 199−205.

(19) Chiuzbăian, S. G.; Schmitt, T.; Matsubara, M.; Kotani, A.; Ghiringhelli, G.; Dallera, C.; Tagliaferri, A.; Braicovich, L.; Scagnoli, V.; Brookes, N. B.; et al. Combining M- and L-edge Resonant Inelastic X-ray Scattering for Studies of 3d Transition Metal Compounds. *Phys. Rev. B: Condens. Matter Mater. Phys.* **2008**, *78*, 245102.

(20) Kurmaev, E. Z.; Ankudinov, A. L.; Rehr, J. J.; Finkelstein, L. D.; Karimov, P. F.; Moewes, A. The L_2:L_3 Intensity Ratio in Soft X-ray Emission Spectra of 3d-metals. *J. Electron Spectrosc. Relat. Phenom.* **2005**, *148*, 1−4.

(21) Okada, K.; Kotani, A. Interatomic and Intra-atomic Configuration Interactions in Core-level X-ray Photoemission Spectra of Late Transition-metal Compounds. *J. Phys. Soc. Jpn.* **1992**, *61*, 4619−4637.

(22) Kikas, A.; Ruus, R.; Saar, A.; Nõmmiste, E.; Käämbre, T.; Sundin, S. Resonant Photoemission of $CoCl_2$. *J. Electron Spectrosc. Relat. Phenom.* **1999**, *103*, 745−749.

(23) van der Laan, G.; Zaanen, J.; Sawatzky, G. A.; Karnatak, R.; Esteva, J.-M. Comparison of X-ray Absorption With X-ray Photoemission of Nickel Dihalides and NiO. *Phys. Rev. B: Condens. Matter Mater. Phys.* **1986**, *33*, 4253−4263.

(24) van der Laan, G.; Zaanen, J.; Sawatzky, G. A.; Karnatak, R.; Esteva, J.-M. Correlation Effect, Charge-Transfer Energy and Covalency in Nickel Compounds as Determined by X-ray Absorption Spectroscopy. *Solid State Commun.* **1985**, *56*, 673−676.

(25) Wyckoff, R. W. G. *Crystal Structures*; John Wiley: New York, 1963.

(26) Costa, M. M. R.; Paixão, J. A.; de Almeida, M. J. M.; Andrade, L. C. R. Charge Densities of Two Rutile Structures: NiF_2 and CoF_2. *Acta Crystallogr., Sect. B: Struct. Sci.* **1993**, *49*, 591−599.

(27) Ramos, C. A.; Lederman, D.; King, A. R.; Jaccarino, V. New Antiferromagnetic Insulator Superlattices: Structural and Magnetic Characterization of $(FeF_2)_m(CoF_2)_n$. *Phys. Rev. Lett.* **1990**, *65*, 2913−2915.

(28) van Uitert, L. G.; Williams, H. J.; Sherwood, R. C.; Rubin, J. J. Graphical Correlation of the Néel Temperatures of Chlorides, Bromides, and Iodides of Divalent 3d Transition Metal Ions. *J. Appl. Phys.* **1965**, *36*, 1029−1030.

(29) Macfarlane, R. M. Raman Light Scattering from Excitons and Magnons in Cobalt Fluoride. *Phys. Rev. Lett.* **1970**, *25*, 1454−1457.

(30) Meng, X.; Deng, J.; Zhu, J.; Bi, H.; Kan, E.; Wang, X. Cobalt Sulfide/Graphene Composite Hydrogel as Electrode for High-performance Pseudocapacitors. *Sci. Rep.* **2016**, *6*, 21717.

(31) Tao, F.; Zhao, Y.-Q.; Zhang, G.-Q.; Li, H.-L. Electrochemical Characterization on Cobalt Sulfide for Electrochemical Supercapacitors. *Electrochem. Commun.* **2007**, *9*, 1282−1287.

(32) Kornienko, N.; Resasco, J.; Becknell, N.; Jiang, C.-M.; Liu, Y.-S.; Nie, K.; Sun, X.; Guo, J.; Leone, S. R.; Yang, P. Operando Spectroscopic Analysis of an Amorphous Cobalt Sulfide Hydrogen Evolution Electrocatalyst. *J. Am. Chem. Soc.* **2015**, *137*, 7448−7455.

(33) Merki, D.; Fierro, S.; Vrubel, H.; Hu, X. Amorphous Molybdenum Sulfide Films as Catalysts for Electrochemical Hydrogen Production in Water. *Chem. Sci.* **2011**, *2*, 1262−1267.

(34) Faber, M. S.; Park, K.; Cabán-Acevedo, M.; Santra, P. K.; Jin, S. Earth-abundant Cobalt Pyrite (CoS_2) Thin Film on Glass as a Robust, High-performance Counter Electrode for Quantum Dot-Sensitized Solar Cells. *J. Phys. Chem. Lett.* **2013**, *4*, 1843−1849.

(35) Sugiura, C.; Gohshi, Y.; Suzuki, I. Sulfur K_β X-ray Emission Spectra and Electronic Structures of some Metal Sulfides. *Phys. Rev. B* **1974**, *10*, 338−343.

DOI: 10.1021/acs.jpcc.7b06882
J. Phys. Chem. C 2017, 121, 24919−24928

(36) McCloskey, B. D.; Valery, A.; Luntz, A. C.; Gowda, S. R.; Wallraff, G. M.; Garcia, J. M.; Mori, T.; Krupp, L. E. Combining Accurate O_2 and Li_2O_2 Assays to Separate Discharge and Charge Stability Limitations in Nonaqueous Li-O_2 Batteries. *J. Phys. Chem. Lett.* **2013**, *4*, 2989−2993.
(37) Fuggle, J. C.; Mårtensson, N. Core-level Binding Energies in Metals. *J. Electron Spectrosc. Relat. Phenom.* **1980**, *21*, 275−281.
(38) Ghiringhelli, G.; Piazzalunga, A.; Dallera, C.; Trezzi, G.; Braicovich, L.; Schmitt, T.; Strocov, V. N.; Betemps, R.; Patthey, L.; Wang, X.; et al. SAXES, a High Resolution Spectrometer for Resonant X-ray Emission in the 400−1600 eV Energy Range. *Rev. Sci. Instrum.* **2006**, *77*, 113108.
(39) van Schooneveld, M. M.; DeBeer, S. A close look at dose: Toward L-edge XAS Spectral Uniformity, Dose Quantification and Prediction of Metal Ion Photoreduction. *J. Electron Spectrosc. Relat. Phenom.* **2015**, *198*, 31−56.
(40) Kramers, H. A.; Heisenberg, W. Über die Streuung von Strahlung durch Atome. *Z. Phys.* **1925**, *31*, 681.
(41) Cowan, R. D. Theoretical Calculation of Atomic Spectra Using Digital Computers. *J. Opt. Soc. Am.* **1968**, *58*, 808−818.
(42) Thole, B. T.; van der Laan, G.; Butler, P. H. Spin-mixed Ground State of Fe Phthalocyanine and the Temperature-dependent Branching Ratio in X-ray Absorption Spectroscopy. *Chem. Phys. Lett.* **1988**, *149*, 295−299.
(43) Green, R. J. Transition Metal Impurities in Semiconductors: Induced Magnetism and Band Gap Engineering. Ph.D. Thesis, University of Saskatchewan, Saskatoon, 2013.
(44) Stavitski, E.; de Groot, F. M. F. The CTM4XAS Program for EELS and XAS Spectral Shape Analysis of Transition Metal L Edges. *Micron* **2010**, *41*, 687−694.
(45) Glatzel, P. *Computer Code*; European Synchrotron Radiation Facility: Grenoble, France.
(46) Delgado-Jaime, M. U.; Zhang, K.; Vura-Weis, J.; de Groot, F. M. F. CTM4DOC: Electronic Structure Analysis from X-ray Spectroscopy. *J. Synchrotron Radiat.* **2016**, *23*, 1264−1271.
(47) Slater, J. C. The Theory of Complex Spectra. *Phys. Rev.* **1929**, *34*, 1293−1322.
(48) Cowan, R. D. *The Theory of Atomic Structure and Spectra*; University of California Press: Berkeley, CA, 1981.
(49) Green, R. J.; Zatsepin, D. A.; St. Onge, D. J.; Kurmaev, E. Z.; Gavrilov, N. V.; Zatsepin, A. F.; Moewes, A. Electronic Band Gap Reduction and Intense Luminescence in Co and Mn Ion-implanted SiO_2. *J. Appl. Phys.* **2014**, *115*, 103708.
(50) Anderson, P. W. Localized Magnetic States in Metals. *Phys. Rev.* **1961**, *124*, 41−53.
(51) van Schooneveld, M. M.; Kurian, R.; Juhin, A.; Zhou, K.; Schlappa, J.; Strocov, V. N.; Schmitt, T.; de Groot, F. M. F. Electronic Structure of CoO Nanocrystals and a Single Crystal Probed by Resonant X-ray Emission Spectroscopy. *J. Phys. Chem. C* **2012**, *116*, 15218−15230.
(52) Cramer, S. P.; de Groot, F. M. F.; Ma, Y.; Chen, C. T.; Sette, F.; Kipke, C. A.; Eichhorn, D. M.; Chan, M. K.; Armstrong, W. H.; Libby, E.; et al. Ligand Field Strengths and Oxidation States from Manganese L-edge Spectroscopy. *J. Am. Chem. Soc.* **1991**, *113*, 7937−7940.
(53) van Schooneveld, M. M.; Gosselink, R. W.; Eggenhuisen, T. M.; Samarai, M. A.; Monney, C.; Zhou, K. J.; Schmitt, T.; de Groot, F. M. F. A Multispectroscopic Study of 3d Orbitals in Cobalt Carboxylates: The High Sensitivity of 2p3d Resonant X-ray Emission Spectroscopy to the Ligand Field. *Angew. Chem., Int. Ed.* **2013**, *52*, 1170−1174.
(54) Haverkort, M. W.; Zwierzycki, M.; Andersen, O. K. Multiplet Ligand-field Theory Using Wannier Orbitals. *Phys. Rev. B: Condens. Matter Mater. Phys.* **2012**, *85*, 165113.
(55) de Groot, F. M. F.; Arrio, M. A.; Sainctavit, Ph.; Cartier, Ch.; Chen, C. T. Fluorescence Yield Detection: Why it does not Measure the X-ray Absorption Cross Section. *Solid State Commun.* **1994**, *92*, 991−995.
(56) de Groot, F. M. F.; Ruus, R.; Elango, M. Charge-transfer Multiplet Analysis of the Resonant 2g3p3p Auger Spectra of CaF_2. *Phys. Rev. B: Condens. Matter Mater. Phys.* **1995**, *51*, 14062−14068.
(57) Krause, M. O.; Oliver, J. H. Natural Widths of Atomic *K* and *L* Levels, K_α X-ray Lines and Several *KLL* Auger Lines. *J. Phys. Chem. Ref. Data* **1979**, *8*, 329−338.
(58) Wasinger, E. C.; de Groot, F. M. F.; Hedman, B.; Hodgson, K. O.; Solomon, E. I. L-edge X-ray Absorption Spectroscopy of Non-heme Iron Sites: Experimental Determination of Differential Orbital Covalency. *J. Am. Chem. Soc.* **2003**, *125*, 12894−12906.
(59) Miedema, P. S.; Borgatti, F.; Offi, F.; Panaccione, G.; de Groot, F. M. F. Iron 1s X-ray Photoemission of Fe_2O_3. *J. Electron Spectrosc. Relat. Phenom.* **2015**, *203*, 8−13.
(60) Kurmaev, E. Z.; McLeod, J. A.; Buling, A.; Skorikov, N. A.; Moewes, A.; Neumann, M.; Korotin, M. A.; Izyumov, Yu. A.; Ni, N.; Canfield, P. C. Contribution of Fe 3d States to the Fermi Level of $CaFe_2As_2$. *Phys. Rev. B: Condens. Matter Mater. Phys.* **2009**, *80*, 054508.
(61) Kurmaev, E. Z.; McLeod, J. A.; Skorikov, N. A.; Finkelstein, L. D.; Moewes, A.; Izyumov, Yu. A.; Clarke, S. Identifying Valence Structure in LiFeAs and NaFeAs With Core-level Spectroscopy. *J. Phys.: Condens. Matter* **2009**, *21*, 345701.
(62) McLeod, J. A.; Buling, A.; Green, R. J.; Boyko, T. D.; Skorikov, N. A.; Kurmaev, E. Z.; Neumann, M.; Finkelstein, L. D.; Ni, N.; Thaler, A.; et al. Effect of 3d Doping on the Electronic Structure of $BaFe_2As_2$. *J. Phys.: Condens. Matter* **2012**, *24*, 215501.

DOI: 10.1021/acs.jpcc.7b06882
J. Phys. Chem. C 2017, 121, 24919−24928